

# On CFD simulation of wind-induced airflow in narrow ventilated facade cavities: coupled and decoupled simulations and modelling limitations

K. Nore <sup>(a,b)</sup>, B. Blocken <sup>(c)</sup> \*, J.V. Thue <sup>(a)</sup>

(a) *Department of Civil and Transport Engineering, Norwegian University of Science and Technology (NTNU), Høgskoleringen 7A, 7491 Trondheim, Norway*

(b) *SINTEF Building and Infrastructure, 7465 Trondheim, Norway*

(c) *Building Physics and Systems, Eindhoven University of Technology, P.O. box 513, 5600 MB Eindhoven, The Netherlands*

## Abstract

Heat and mass transfer modelling in building facades with ventilated cavities requires information on the cavity air change rates, which can be a complex function of the building geometry and meteorological conditions. This paper applies Reynolds-averaged Navier-Stokes (RANS) CFD to study wind-induced airflow in the narrow (23 mm) ventilated facade cavities of a low-rise building by coupled and decoupled simulations. In the coupled simulations, the wind-flow pattern around the building and the resulting air flow in the cavities are calculated simultaneously and within the same computational domain. In the decoupled simulations, two separate CFD simulations are conducted: a simulation of the wind flow around the building (with closed cavities) to determine the surface pressures at the cavity inlet and outlet openings, and a simulation of the cavity airflow, driven by these surface pressures. CFD validation is performed for the external and internal (cavity) flows. It shows that while both laminar and turbulent cavity airflow can be accurately reproduced with low-Reynolds number modelling, this method fails in the transitional regime. The valid CFD results (outside the transitional regime) are analysed in terms of cavity air flow patterns and air change rates per hour (ACH) for different cavity positions, wind speeds and wind directions. The CFD results of cavity air speed and ACH compare favourably with values from previous experimental studies. The coupled and decoupled simulation results provide an indication of the local losses. Future work should focus on adapting RANS CFD low-Re-number models to accurately model cavity flow in the transitional regime.

**Keywords:** Cavity ventilation; Building envelope; Computational Fluid Dynamics; Numerical simulation; Pressure loss

## Nomenclature

$C$	local loss coefficient
$C_p$	pressure coefficient
$C_s$	roughness constant
$C_\mu$	variable in realizable k- $\epsilon$ model
$d$	cavity depth (m)
$D_h$	hydraulic diameter (m)
$f$	friction factor
$k$	turbulent kinetic energy ( $m^2/s^2$ )
$k_{non-c}$	correction factor for non-circular cross-sections
$k_s$	equivalent sand-grain roughness height (m)
$L, W, H$	length, width, height (m)
$n$	air change rate (1/h)
$P$	pressure (Pa)
$Re$	cavity Reynolds number
$Re_z$	wall-distance based Reynolds number
$u^*$	friction velocity (m/s)
$u^*_{ABL}$	friction velocity associated with the inlet profiles of $U$ , $k$ and $\epsilon$ (m/s)
$U$	streamwise component of the mean wind-velocity vector (m/s)
$U_H$	wind speed in upstream undisturbed flow at building height (m/s)

---

\* Corresponding author: Bert Blocken, Building Physics and Systems, Eindhoven University of Technology, P.O.Box 513, 5600 MB Eindhoven, the Netherlands. Tel.: +31 (0)40 247 2138, Fax +31 (0)40 243 8595  
E-mail address: b.j.e.blocken@tue.nl

$U_{10}$	reference wind speed at 10 m height in the upstream undisturbed flow (m/s)
$W$	vertical component of the mean wind-velocity vector (m/s)
$x$	coordinate along building facade (m)
$z$	height (m)
$z_p$	distance between the centre point P of the wall-adjacent cell and the wall (m)
$z_0$	aerodynamic roughness length (m)
$z^+$	dimensionless wall unit
$z^*$	dimensionless wall unit

#### *Greek symbols*

$\Delta$	difference
$\varepsilon$	turbulence dissipation rate ( $m^2/s^3$ )
$\theta$	angle between the reference wind direction and the normal to the facade ( $^\circ$ )
$\kappa$	von Karman constant ( $\approx 0.42$ )
$\nu$	kinematic viscosity ( $m^2/s$ )
$\rho$	air density ( $kg/m^3$ )

#### *Abbreviations*

ABL	Atmospheric Boundary Layer
ACH	Air change rate per hour
CFD	Computational Fluid Dynamics
RANS	Reynolds-averaged Navier-Stokes
SIMPLE	Semi-Implicit Method for Pressure Linked Equations

#### *Subscripts*

avg	averaged
D	computational domain
P	centre point of the wall-adjacent cell

## **1. Introduction**

Analysis of the hygrothermal behaviour of ventilated cavity walls requires information on the cavity air change rates as a function of the influencing parameters. Cavity ventilation can be driven by wind (forced convection) or by local density differences due to buoyancy (natural convection). The resulting pressure differences can drive airflow through the cavity when they can overcome the local losses and the friction losses in the cavity. The local losses consist of the entrance and exit losses. Wind pressure on a windward building facade generally increases from bottom to top, and will cause a downward cavity flow. Buoyancy on the other hand will generally cause an upward flow. The resulting flow direction and cavity ventilation rate will depend on the interaction between both driving forces.

In general, the cavity air change rate per hour (ACH) depends on a wide range of parameters including building geometry, environment topography, position and size of the cavity openings in the facade, cavity dimensions, cavity wall roughness, permeability of the cladding, wind speed, wind direction, temperature and cavity Reynolds number. Numerical heat-air-moisture (HAM) transfer models for building facades with ventilated cavities require detailed information on cavity air flow to calculate the transfer of heat and moisture to and from the inside cavity wall surfaces [1-4]. This type of information can be obtained from full-scale measurements [5-12], theoretical models [10-11,13] or numerical simulations with Computational Fluid Dynamics (CFD) [1,3,11]. While much work has been done on natural and forced ventilation of buildings (indoor) and of wide ventilated cavities (e.g., double-skin facades), much less effort has been devoted to the ventilation of narrow facade cavities such as those found in a rainscreen-type wall. Most previous work on ventilation for this type of walls has been experimental and theoretical, and CFD studies are very scarce. A literature review of cavity wall ventilation studies, up to 2004, has been provided by Straube et al. [10].

In the past, a number of full-scale measurements of cavity air speed and/or ACH and of the corresponding exterior wind speed, wind direction and surface pressures and exterior-interior temperature differences have been performed both on site, for real buildings [5-10], and in laboratory conditions, on wall specimens [10-12]. They have indicated the importance of both wind and buoyancy as driving forces for cavity ventilation and they have also provided information on the ACH and cavity air speeds for those specific building and cavity geometries. However, both on-site measurements and laboratory tests have a number of important disadvantages. The interpretation of on-site measurement results is complicated by the uncontrolled meteorological conditions during the measurements and the possibility of combined occurrence of wind and

buoyancy, which can counteract each other. This makes it hard to analyse the influence of each individual parameter and to draw general conclusions. Laboratory measurements allow a much larger control of the influencing parameters, but the inlet and outlet conditions for the cavity flow are generally strongly simplified, and the complexity of the wind-flow pattern around the building is not taken into account.

Cavity airflow rates can also be assessed by theoretical equations such as the Darcy-Weisbach equation that relates pressure differences to airflow rates, and in which a distinction is made between friction losses and local losses, such as entrance and exit losses [14,15]. For wind-induced ventilation, the wind pressures at the positions of the cavity openings are needed as input to this equation. They are either measured on site or in reduced-scale wind tunnel experiments, or extracted from existing databases or analytical equations (for a review on pressure coefficient data in building simulation, see [16]). There are two main problems associated with this approach. First, detailed pressure coefficient ( $C_p$ ) data in databases are often only available for buildings with a simplified geometry that can be very different from the actual building under study. Second, the entrance and exit losses are generally not known. Although hydraulic resistance data sets [e.g., 14,15] provide standard values for simplified inlet and outlet geometries, they often do not provide values for the actual inlet and outlet geometries of building wall cavities. They generally also do not provide information on the variation of the local losses with wind direction.

Apart from measurements and theoretical equations, cavity ventilation can also be studied by CFD. Up to now, only a few efforts have been made in this direction [1,3,11]. CFD simulations can be performed in a coupled or a decoupled way. In the coupled simulations, the atmospheric boundary layer wind-flow pattern around the building and the resulting air flow in the cavities are calculated simultaneously and within the same computational domain. In the decoupled simulations, two separate CFD simulations are made: a simulation of the outdoor wind flow around the building (with closed cavities) to determine the surface pressures at the position of the cavity inlet and outlet openings, and a simulation of the cavity air flow, driven by these surface pressures. Pinon et al. [11] performed isothermal CFD simulations of the air flow in different types of cavities and with different inlet conditions. The simulations were made in a decoupled way, i.e. excluding simulation of the wind flow around the building. Stovall and Karagiozis [1] conducted thermal CFD simulations in different cavities and with different wind speed and temperature differences. To some extent, these simulations were coupled with the outdoor wind flow, however only a relatively small outdoor air volume ( $L \times W \times H = 0.5 \times 0.36 \times 2.43 \text{ m}^3$ ) was considered, and the specific features of wind flow around the building were not included. Gnoth et al. [3] have recently extended a HAM model with CFD to analyse “cavity fluid dynamics (CaFD)”, allowing simulation of laminar convective heat and moisture transfer in cavities. Also in these simulations, the outdoor wind flow was not considered.

At present, there are a number of open issues concerning cavity ventilation in general and CFD simulations of cavity ventilation in particular. There is very little information about cavity ACH and air flow patterns. Up to now, to the knowledge of the authors, fully coupled CFD simulations of the atmospheric boundary layer wind-flow pattern around buildings and the resulting air flow in the cavities have not yet been performed. This type of studies is required for detailed and systematic investigations of cavity ACH and air flow patterns as a function of influencing parameters. There is also very little information on local losses for facade cavities. An investigation of the local losses in cavities requires the combination of both coupled and decoupled simulations. However, first and foremost, the accuracy and reliability of CFD for cavity ventilation studies should be investigated. As such studies can encompass laminar, transitional and turbulent cavity flow, it should be examined to what extent RANS CFD can accurately reproduce these flow regimes.

This paper presents a CFD investigation of wind-induced air flow in the narrow (23 mm) ventilated facade cavities of an isolated low-rise building, based on coupled and decoupled simulations. CFD validation is performed for the building surface pressures and for the interior cavity flow. The results of the study are presented in terms of cavity air flow patterns and cavity ACH for different cavity positions, wind speed and wind directions. The coupled and decoupled simulations are compared to provide an indication of the local losses. Based on the validation studies, some CFD modelling limitations for this type of studies can be identified.

The paper consists of 9 sections. In section 2, the geometry of the low-rise building model is described. Section 3 contains some considerations for coupled outdoor wind flow and cavity airflow simulations. Section 4 presents the validation studies. In section 5, the coupled and decoupled simulations are outlined. Section 6 presents the simulation results. In section 7, the CFD results are compared with results from previous experimental studies. Sections 8 (discussion) and 9 (summary and conclusions) conclude the paper.

## **2. Building model**

The geometry of the building model is for a large part based on that of the low-rise rectangular test building of SINTEF Building and Infrastructure and the Norwegian University of Science and Technology

(NTNU) in Voll, Trondheim, Norway. It has dimensions  $L \times W \times H = 11.3 \times 4.8 \times 4.3 \text{ m}^3$  and a roof overhang with a length of 0.34 m and a height of 0.3 m (Fig. 1). The long front and back facades each consist of 17 ventilated cavities. Each cavity has a height of 3.495 m and a horizontal linear inlet and outlet slot over the entire width of the cavity (Fig. 1). The cavities are separated from each other by vertical wooden battens, some of which have different cross-sectional dimensions. A wooden cladding of 19 mm thickness separates the cavities from the outdoor environment. In this study, the cavity depth is 23 mm and the cladding itself is assumed airtight. The building is considered to be isolated (no surrounding buildings, trees, etc.) and positioned on flat, uniformly rough terrain covered with short grass (aerodynamic roughness length  $z_0 = 0.03 \text{ m}$  [17]). Fig. 1c is a detailed view of the vertical cross-section of the top and bottom of the cavity. The bottom cavity opening is 400 mm above ground level, and the top opening is 35 mm below the roof overhang. The vertical batten also starts at 400 mm below ground level, but extends all the way up to the roof overhang. This configuration represents the computational geometry for the “fully coupled” approach (configuration A). For the decoupled approach, this configuration is decomposed into two separate configurations: configuration B, in which the cavity is closed, and configuration C, which only represents the cavity (Fig. 2).

### 3. Considerations for coupled outdoor wind flow and cavity airflow simulations

For the specific geometry of the cavity openings of the building (opening just below roof overhang and opening adjacent to wall at a certain distance from the ground surface), no standard values for local loss coefficients could be found in hydraulic resistance data sets [e.g. 14,15]. This motivates the coupled CFD approach.

The flow around the building is fully turbulent, apart from the small viscosity-affected regions in the boundary layer near the building surfaces and ground surfaces in the domain. The flow in the cavities however can be laminar, transitional or turbulent, depending on the cavity Reynolds number and on wall roughness and entrance effects. The coupled simulations need to consider the possibility of these different flow regimes occurring within the same computational domain.

The commonly used approach in wind engineering for building aerodynamics is based on the Reynolds-averaged Navier-Stokes (RANS) equations [18,19]. The turbulence models used in this approach, such as the  $k$ - $\epsilon$  models and the Reynolds Stress model, are generally high-Reynolds number models that are only valid in the turbulent region of the flow. For the boundary layer region, which contains the inner layer including the thin viscous sublayer, the buffer layer and the logarithmic layer, modelling adjustments need to be made. The two main options are low-Reynolds number modelling and wall-function modelling. Low-Re number modelling refers to resolving the whole boundary layer by placing cells in each part of it. Wall functions are semi-empirical formulae that bridge the region between the wall and the logarithmic layer, and that provide an approximation of the effect of the wall on the mean wind speed and turbulence quantities in the logarithmic layer. Low-Reynolds number modelling requires much finer grids than wall-function modelling. The near-wall grid resolution can be expressed by the  $z^*$  value:  $z^* = u^* z_p / \nu$  [20,21], where  $u^*$  ( $= C_\mu^{1/4} k_p^{1/2}$ ) is the friction velocity,  $z_p$  is the distance from the centre point P of the wall-adjacent cell to the wall, and  $\nu$  is the kinematic viscosity. The friction velocity is based on the turbulent kinetic energy  $k_p$  in the point P and on  $C_\mu$ . Note that in many commercial CFD codes,  $z^*$  is used instead of the traditional wall unit  $z^+$ , because of reasons explained in [20,22]. Appropriate grids for low-Re number modelling have a  $z^*$  value below 4 or 5 to ensure that the point P is situated in the viscous sublayer. Preferably,  $z^* = 1$  to have at least a few cells inside the viscous sublayer [18,20,21]. Wall-function grids should have a  $z^*$  above 20-30 and below 300-500 to ensure that P is situated in the logarithmic layer [18,20,21].

Modelling the wind flow around buildings is typically performed by combining a high-Re number model with wall functions [18,19]. Modelling the flow in the narrow facade cavities however requires low-Re number modelling. In the commercial CFD code Fluent 6.3.26 used in this study [21], low-Re number modelling refers to a two-layer zonal approach, that divides the computational domain into two regions: the viscosity-affected region and the fully-turbulent region. The demarcation between both regions is determined by the wall-distance based turbulent Reynolds number,  $Re_z = zk^{1/2}/\nu$ , where  $z$  is the normal distance from the wall at the cell centres and  $k$  is the turbulent kinetic energy. Where  $Re_z > 200$ , the high-Re number model is used. Where  $Re_z < 200$ , the one-equation Wolfhstein model [23] is employed.

For the coupled simulations in this study, the combination of the high-Re number realizable  $k$ - $\epsilon$  model [24] with the so-called “enhanced wall treatment” [21] will be employed. Enhanced wall treatment refers to the approach in which the two-layer zonal model is combined with enhanced wall functions. This approach is identical to the two-layer zonal approach when the grid is fine enough (typically  $z^* = 1$ ), and provides improved accuracy for those regions where the grid is not fine enough. The aim in generating the grid for the coupled simulation is to have  $z^* < 1$  in the cavity and near the cavity entrance and exit. For the remainder of the walls in the computational domain, such as the exterior building surfaces, along which higher wind

velocities are present, keeping  $z^* < 1$  would lead to an unnecessary and excessively fine grid with cell sizes down to a few hundred micrometers [25].

#### 4. CFD validation

Different options could be pursued for CFD validation. The most straightforward option would be to use experimental data of wind speed around the building, surface pressures on the facade, and cavity air speed and ACH for the building under study. However, because of several practical reasons, this was not an option. The most important are (1) the fact that the geometry of the cavities is variable in time (as new test walls with different cavity geometries are regularly installed) and (2) the fact that even at a given moment in time, the cavities have different geometries. Therefore, the building in the present study is a simplified version of the real building, in which all cavities have the same depth and height and the same type of inlet and outlet openings. This limits the number of variables involved and allows an analysis of the ACH as a function of cavity position in the facade, without the results being obscured by additional geometrical parameters.

Instead, it was chosen to perform generic sub-configuration validation [18,26]. This method implies decomposition of the actual problem or configuration into simpler, generic problems or configurations, which contain at least part of the features of the flow in the actual configuration. Validation is then performed for the generic sub-configurations, for which often high-quality experimental data are available in the literature. If the numerical model performs well for these configurations, it can reasonably be assumed that it will also provide reliable predictions for the more complex building configuration. An advantage of the sub-configuration validation is that it allows a step-by-step analysis of the performance of CFD, which will allow to clearly identify modelling limitations.

The sub-configuration validation consists of three parts: (1) wind velocity pattern around a cubic building; (2) wind pressure distributions on the surfaces of a cubic building; and (3) laminar, transitional and turbulent flow in a channel. Focusing on the cubic building is justified because the flow around this basic type of bluff body contains the salient features of the flow that will also occur around the building model in Fig. 1. Because the first part of the validation study has been reported in detail in an earlier paper [25], in which a good qualitative and quantitative agreement was found, it is not repeated here, and only the two other parts are described below.

##### 4.1. Mean surface pressures

Wind tunnel measurements of pressure distributions on the surfaces of a cubic (0.15 m) building model were reported by Richards et al. [27]. The tests were conducted in the University of Auckland boundary layer wind tunnel, at a scale of 1:40 and for different wind directions. The maximum blockage ratio is 1.6 %. The boundary layer up to two building heights was well matched by a log law with  $z_0 = 0.42$  mm (= 16.8 mm in full scale). Mean wind speed at cube height,  $U_H$ , was 6.4 m/s, yielding a building Reynolds number of about 65,000, which is well above the limit 11,000 for Reynolds number independent flow [28]. The undisturbed vertical profiles of mean wind speed and turbulence were measured in the empty wind tunnel (with roughness elements but without building present). The exact measurement location at the turntable however is not known. Ideally, this location should be that at which the building will be positioned. Recent research has shown that reference measurements further upstream can to some extent lack representativeness due to the development of an internal boundary layer over the smooth surface of wind tunnel turntable [29]. The pressure measurements were made along the intersection of the cube with the vertical centre plane and with a horizontal plane at half the cube height ( $z = H/2$ ), among other positions. More information on the experiments can be found in Richards et al. [27].

3D steady RANS simulations are performed at model scale. The computational domain has dimensions  $L_D \times W_D \times H_D = 21H \times 21H \times 10H$ . The building model is placed at  $5H$  from the inlet, yielding a downstream distance of  $15H$ . A structured grid is used with grid resolution determined by grid-sensitivity analysis on three different grids with a refinement factor  $\sqrt{2}$ . The resulting grid has 207,980 cells (Fig. 3). 24 cells are used along the building edges. Both for the building walls and the bottom of the domain, the distance  $z_p$  is  $0.005H$ , yielding  $z^*$  values in the range 30-90, apart from the intersection of the building surfaces with the bottom of the domain, where  $z^*$  is lower than 30. Fluent 6.3.26 is used to solve the 3D RANS equations and the realizable  $k-\epsilon$  model equations [24]. Pressure-velocity coupling is taken care of by the SIMPLE algorithm. Standard pressure interpolation is used. Second order discretization schemes are used for both the convection terms and the viscous terms of the governing equations.

Simulations are made for two wind directions:  $\theta = 0^\circ$  (wind direction perpendicular to the surface) and  $45^\circ$  (Fig. 3). The vertical boundary planes of the domain have different types of boundary conditions depending on the wind direction (Fig. 3). In the case of  $\theta = 0^\circ$ , plane 1 is the inlet plane, plane 3 the outlet plane and

planes 2 and 4 are the side planes. For  $\theta = 45^\circ$ , planes 1 and 2 are the inlet planes and planes 3 and 4 are the outlet planes. The side planes (for  $\theta = 0^\circ$ ) and the top of the computational domain are modelled as slip walls (zero normal velocity and zero normal gradients of all variables). At the outlet(s), zero static pressure is specified. At the inlet plane(s), the vertical profiles of mean wind speed, turbulent kinetic energy  $k$  and turbulence dissipation rate  $\varepsilon$  are imposed. The vertical inlet profile of mean wind speed is equal to the measured one [27]. The turbulent kinetic energy profile was obtained from the measured turbulence intensities, and turbulence dissipation rate  $\varepsilon = (u^*_{ABL})^3/\kappa(z+z_0)$  with  $u^*_{ABL} = 0.46$  m/s. For the ground boundary condition, the standard wall functions by Launder and Spalding [30] with roughness modifications by Cebeci and Bradshaw [31] are used. The values of the equivalent sand-grain roughness height  $k_s$  and roughness constant  $C_s$  needed in these wall functions are obtained based on the aerodynamic roughness length  $z_0 (= 0.42$  mm) by the function derived by Blocken et al. [32] for Fluent 6 (up to at least version 6.3):

$$k_s = \frac{9.793 z_0}{C_s} \quad (1)$$

The values used are  $k_s = 0.0008$  m and  $C_s = 5$ . Note that for fully aerodynamically rough walls, only the value of the product  $C_s k_s$ , and not the values of the individual parameters, determine the wall function values [21,32].

Fig. 4 displays measured and simulated pressure coefficients  $C_p$ , for  $\theta = 0^\circ$  and  $45^\circ$ , along the intersections of the cube surfaces with a vertical centre plane and the horizontal plane at  $z = H/2$ . The pressure coefficients are calculated with reference wind speed  $U_H = 6.4$  m/s. Figs. 4a and c each show two sets of measurement data. The difference between both sets is caused by the effect of the pressure tappings in one roof corner (quarter of the roof), see [27]. Richards et al. [27] also mention that the model was slightly misaligned in the wind tunnel, causing some asymmetry in the results, as shown in Figs. 4b and d. Comparing the CFD results with the wind tunnel data shows that:

- (1) Fig. 4a:  $C_p$  at the upper part of the windward facade is predicted very well, while at the lower part, underestimations go up to a maximum of 25%. On the roof, the absolute value near the upwind edge is overestimated (15%), but larger errors (underestimations) are found for the rest of the roof (up to 100%). Values at the leeward facade are about half those of the measurements.
- (2) Fig. 4b: The agreement between simulated and measured  $C_p$  at the windward facade is very good. Large underestimations however are found at the side and leeward faces (up to 100%).
- (3) Fig. 4c: Again, the agreement at the windward facade is very good. On the roof, a 40% underestimation is present at the upwind edge, but a significantly better agreement is found for the rest of the roof. A quite good agreement is also seen at the leeward facades (max. deviation is 20%).
- (4) Fig. 4d: A good overall agreement is observed at both windward and leeward facades. The deviation along line "01" is partly due to misalignment of the model. Deviations at the leeward facades are lower than 25%.

The deviations at the roof, the side facades and the leeward facade are for a large part attributed to the fact that steady RANS is not capable of modelling the inherently transient nature of separation, recirculation and of vortex shedding in the wake. Therefore, calculation results in these regions are generally deficient [33,34]. However, both the validation study in [25] and the validation study in this paper show that steady RANS with the realizable  $k$ - $\varepsilon$  model seems to provide quite accurate results for the windward facade. Note that the focus will be on the windward facade and on wind directions  $0^\circ$  and  $22.5^\circ$  only. Results for e.g.  $\theta = 67.5^\circ$  and  $90^\circ$ , when this facade is (partly) in the region of separated flow, are not considered reliable.

#### 4.2. Laminar, transitional and turbulent channel flow

A distinction is made between developing and fully-developed channel flow. For fully-developed flow, detailed experimental data are reported in the literature, often in terms of friction coefficients as a function of channel Reynolds number and wall roughness. For developing flow however, unambiguous quantitative information about entrance lengths for laminar and turbulent flow is not available; different sources provide either very different entrance length equations, or provide very wide ranges of possible entrance lengths [14,15,35-37]. The reason for this can be the sensitivity of the entrance length to the inlet conditions (inlet geometry, flow profile, turbulence intensity), wall roughness, etc. For this reason, the validation study here only focuses on fully-developed channel flow.

The pressure loss in fully-developed channel flow (i.e. due to friction) is given by the Darcy-Weisbach equation [14,15]:

$$\Delta P_F = f \frac{L}{D_h} \left( \frac{\rho W_{avg}^2}{2} \right) \quad (2)$$

where  $f$  is the Darcy-Weisbach friction factor,  $L$  is the length of the channel,  $D_h$  is its hydraulic diameter,  $\rho$  is the fluid density and  $W_{avg}$  is the average fluid speed in the cross-section. For fully-developed laminar flow in a pipe with circular cross-section,  $f$  is equal to  $64/Re$ . For fully-developed turbulent flow, the friction loss depends not only on the Reynolds number, but also on the roughness of the pipe. For smooth walls and for Reynolds numbers below  $10^5$ , the turbulent friction factor is well described by the Blasius equation for smooth pipes with circular cross-section:  $f = 0.3164/Re^{0.25}$  [14,35]. This equation is a curve fit to experimental smooth-wall data collected in 1913.

For a channel of non-circular cross-section, generally, Eq. (2) is used with the appropriate hydraulic diameter  $D_h$ . This, however, is only allowed when the thickness of the boundary layer is very small over the entire or almost the entire perimeter of the cross-section compared with the dimensions of the cross-section [14]. Idelchik [14] provides correction factors  $k_{non-c}$  for the friction factor  $f$  for non-circular channels. For laminar flow in a plane slot,  $k_{non-c} = 1.5$ , yielding  $f = 96/Re$ . For turbulent flow in a plane slot,  $k_{non-c} = 1.1$ , yielding  $f = 0.3480/Re^{0.25}$ .

The validation study focuses on the reproduction of the friction losses for fully-developed laminar, transitional and turbulent flow in a smooth pipe with circular cross-section and in a plane slot. The pipe has a diameter of 0.046 m, and the plane slot has a depth of 0.023 m, corresponding to a hydraulic diameter of 0.046 m. The CFD simulations are performed with the RANS equations, the realizable  $k-\epsilon$  model and enhanced wall treatment, i.e. the same combination that will be used for the actual coupled and decoupled simulations in the next section. The simulations are conducted in 2D, because of axial symmetry (for the pipe) and the 2D character of the plane slot (infinite width). The grids are based on grid-sensitivity analysis. Simulations are made for  $Re$  ranging from 100 to  $10^5$ . The results for the friction coefficient  $f$  are presented in a double-logarithmic graph in Fig. 5a, and also in a semi-logarithmic graph in Fig. 5b to allow a better quantitative assessment of the deviations. The following observations are made:

- (1) The simulations correctly predict the friction factor differences (correction factors 1.5 and 1.1) between pipe flow and plane slot flow for low  $Re$  ( $< 500$ ) and high  $Re$  ( $> 10000$ );
- (2) A close agreement is found between CFD simulations and theoretical/empirical expressions for the friction factors for low  $Re$  ( $< 500$ ) and high  $Re$  ( $> 10000$ );
- (3) Large deviations however occur in the intermediate  $Re$  numbers, which are larger than 25% for  $Re = 1000-3500$ , indicating an important modelling discrepancy here. For this reason, in the next section, only results for which the cavity  $Re$  numbers are outside this range will be reported.

## 5. CFD application

CFD simulations are performed for the coupled case (case A) and the decoupled cases (case B and C), see Fig. 2.

### 5.1. Coupled simulations

#### 5.1.1. Geometry and computational grid

Due to the relatively complex geometry of the building with cavities, battens and roof overhang, and the large difference between the smallest (0.023 m) and the largest (about 100 m) length scales in the domain, generating a computational grid with good quality for the coupled simulation is not straightforward. The quality of the grid in the immediate vicinity of the building and in the cavities is considered very important for the coupled simulation. Standard automatic or semi-automatic generation of an unstructured grid allows insufficient control of local grid resolution, grid stretching, control volume skewness and aspect ratio. To allow full control over the grid quality and resolution, the grid is constructed using the grid generation procedure presented by van Hooff and Blocken [38]. This procedure allows to efficiently and simultaneously generate the geometry and the computational grid. It consists of a series of extrusion operations, i.e. creating the geometry and the grid based on geometrical translation operations of pre-meshed 2D cross-sections. In this case, the ground plane of the computational domain is constructed and meshed first, after which it is extruded vertically to generate the 3D geometry and grid. For more details, the reader is referred to ref. [38]. This procedure allows modelling complex geometries with full control over grid quality and grid resolution. This is considered very important here, because the grid resolution near the cavity openings and inside the cavities should be adjusted for low-Reynolds number modelling, as explained in section 3.

The resulting computational domain has dimensions  $L_D \times W_D \times H_D = 110 \times 110 \times 50 \text{ m}^3$ . The building is situated in the corner of the domain, at  $5H$  from both inlet planes (Fig. 6a). Fig. 6b shows the model geometry, including the roof overhang, the individual cavities and the vertical battens separating the cavities. The grid that has been constructed is a hybrid grid, which is fully structured (hexahedral cells) in the cavities and in the immediate vicinity of the building model, and unstructured (prismatic cells) at a larger distance from the building. The grid resolution was determined based on grid-sensitivity analysis, yielding about  $2.6 \times 10^6$  cells with 20 cells across the depth and a minimum of 8 cells along the width of each cavity. In all cavities and for all simulations that will be reported,  $z^*$  was lower than 1. Fig. 6c displays the grid on the surfaces of the building, and Fig. 6d is a detail of the surface grid near the top frontal corner, in which the top cavity openings and the battens can be seen.

### 5.1.2. Solution characteristics and settings

The 3D RANS equations and the equations of the realizable  $k-\varepsilon$  model are solved. Pressure-velocity coupling is taken care of by the SIMPLE algorithm. Pressure interpolation is standard. Second order discretization schemes are used for both the convection terms and the viscous terms of the governing equations. The inlet profiles for mean wind speed, turbulent kinetic energy and turbulence dissipation rate are those by Richards and Hoxey [39], corresponding to  $z_0 = 0.03 \text{ m}$ . Simulations are performed for different reference wind speed  $U_{10}$  and wind directions. The boundary condition settings for outlet, sides and top of the domain are identical to those in section 4.1. For the walls, enhanced wall treatment is applied. It is important to note that “enhanced wall treatment” in Fluent 6.3 implies that all walls are considered smooth (roughness height  $k_s = 0 \text{ m}$ ), also those where the enhanced wall functions are used. The bottom of the computational domain therefore also has zero roughness height, instead of the proper value given by Eq. (1). As a result, there is an inconsistency between the roughness of the inlet profiles ( $z_0 = 0.03 \text{ m}$ ) and the ground roughness in the computational domain, which will lead to a non-horizontally homogeneous atmospheric boundary layer in the simulations [32,40]. This means that streamwise gradients will occur in the vertical inlet profiles of mean wind speed and turbulence quantities. The incident profiles (at the location where the building would be positioned) are therefore different from the inlet profiles. The occurrence of these gradients was tested by a simulation in an empty 2D domain (Fig. 7). They are pronounced for each of the three variables. This does not compromise the value of the simulations, but it should be considered that the results are representative of the incident profiles of the simulation, rather than the inlet profiles.

### 5.2. Decoupled simulations

The decoupled simulations consist of two parts: (1) simulations for the building with closed cavities (case B) and (2) simulations for the cavities (case C) (Fig. 2). The grids are constructed in the same way as explained in section 5.1.1. All solution characteristics and settings are the same as for case A. For case C, two sets of simulations are performed: C1 and C2. In case C1, the pressures at the inlet and outlet openings of the closed cavities (case B) are used as boundary conditions for the simulations in the geometry of case C, leading to a developing flow in the cavity, downstream of the inlet. In case C2, fully-developed velocity profiles are used as inlet boundary conditions for the geometry of case C. Therefore, in case C1, both the friction losses and part of the local losses are included. Case C2 on the other hand only includes friction losses. The results are presented in the next section.

## 6. CFD results

### 6.1. Coupled simulations

Fig. 8 provides an overall view of the flow inside the cavities for  $\theta = 0^\circ$  by illustrating streamlines. The overall flow in the cavities is from top to bottom. A clear flow separation and recirculation occur at the top inlet of the four cavities that are situated closest to the edges. This is attributed to the fact that the velocity vector near this opening has a relatively strong lateral component, i.e. parallel to the windward facade.

Vertical profiles of the ratio  $W/U_{10}$  at the top and bottom of each cavity, for  $U_{10} = 10 \text{ m/s}$  and  $\theta = 0^\circ$  and  $22.5^\circ$  are shown in Fig. 9. Results for more oblique wind directions are not shown because for these directions, the cavity Reynolds numbers dropped into the transitional regime. Fig. 9a (and Fig. 1c) show the positions of the two lines along which the profiles are taken. They are located at the top and bottom cavity opening and in the middle of the cavity depth. Negative velocity ratios indicate downflow. Fig. 9b shows that for  $\theta = 0^\circ$ , both the largest velocities and the largest velocity gradients are found at the edge cavities, in which a highly non-uniform flow occurs. In these edge cavities, a diagonal flow takes place, as indicated by the shift

of the velocity peaks from one cavity edge to the other as the flow moves from top to bottom. At the top opening of these cavities, a small region with upflow occurs. The flow is most uniform in the cavities in the middle of the facade, where the stagnation point at the facade occurs and where the lateral velocities (in x direction) are smallest. Fig. 9c shows that for  $\theta = 22.5^\circ$ , apart from the edge cavities, also most cavities in the middle region demonstrate non-uniform and diagonal flow. Flow non-uniformity appears least pronounced between  $x = 1$  and 2 m (cavity nr. 5), which approximately corresponds to the shifted stagnation point.

Fig. 10 shows profiles of the ratio  $W/U_{10}$  across the depth of the middle cavity (nr. 19) for  $\theta = 0^\circ$ , and for  $U_{10} = 2$  and 10 m/s. For these values of  $U_{10}$ , the cavity Re numbers, based on the average cavity speed, are all below 1000 or above 3500. The values in Fig. 10 are taken in the middle of cavity nr. 19. At the entrance (point A), the profile is skewed towards the inner cavity surface. Travelling downwards, the profile reaches an approximate equilibrium shape (point D), which is maintained until at least point F. At the outlet, the profile is slightly skewed towards the outer cavity surface. The results show a near-parabolic profile (between points D and F) characteristic of laminar flow for  $U_{10} = 2$  m/s and a more uniform (flattened) profile typical for turbulent flow for  $U_{10} = 10$  m/s (also between D and F).

Fig. 11a displays the ratio of the air change rate per hour (ACH)  $n$  (1/h) and  $U_{10}$ , for  $U_{10} = 2$  and 10 m/s. The decrease of this ratio with decreasing  $U_{10}$  is a direct result of the change in cavity flow regime from turbulent to laminar, as shown by the corresponding Re numbers in Fig. 11b. Fig. 11c shows the ratio  $n/U_{10}$  for  $U_{10} = 10$  m/s and for  $\theta = 0^\circ$  and  $22.5^\circ$ . Fig. 11d shows the corresponding Re numbers. As the wind direction becomes more oblique to the facade, the ratio  $n/U_{10}$  shows a general decrease. However, for the cavity at the upwind edge, the value for  $22.5^\circ$  is larger than that for  $0^\circ$ . Similar observations of maxima occurring for slightly oblique instead of perpendicular angles were made in the past concerning pedestrian-level wind conditions around buildings [29,41] and wind-driven rain deposition on building facades [42,43]. These observations could be attributed to changes in the upstream wind-flow pattern, i.e. the so-called wind-blocking effect [29,44,45], due to the changed stagnation region.

## 6.2. Decoupled simulations

The wind-flow simulations for case B yield the static pressures  $P$  at the position of the inlet and outlet openings. These values can be converted to pressure coefficients by  $C_p = (P - P_0)/0.5\rho U_{10}^2$ , where  $P_0$  is the reference pressure and  $\rho$  the air density (1.225 kg/m<sup>3</sup>). Fig. 12a displays  $C_p$  for the top (highest value) and bottom (lowest value) of every cavity, and for the two wind directions. The  $C_p$  distribution at the top is quite uniform along the length for  $\theta = 0^\circ$ , while for  $\theta = 22.5^\circ$ ,  $C_p$  shows a pronounced maximum for the cavity at the upwind edge.

The pressures from case B are used to calculate cavity flow rates for case C1. The decoupled simulations for case B+C1 provide significant overestimations of the ACH compared to the coupled simulations of case A (Fig. 12b). The overestimations range from 26% to 40% for  $\theta = 0^\circ$  and from 34 to 57% for  $\theta = 22.5^\circ$ . They are caused by the important simplifications associated with decoupled simulations. In these simulations, the only information transferred from case B to case C1 are the pressure coefficients. The simulations in case C1 do not take into account the actual local direction of the wind velocity vectors near and in the openings and the occasional flow separation and recirculation in the cavities. Instead, only vertical cavity air flow is considered along the entire cavity. As a result, case B+C1 only partly reproduces the local losses that are simulated in case A.

## 6.3. Local pressure losses

As mentioned in the introduction, one of the open issues in cavity ventilation is that there is very little information on local losses for facade cavities. Hydraulic resistance data sets often do not cover the geometrical complexity of actual inlet and outlet openings of building wall cavities. In particular, for the present building, loss coefficients could not be found in such data sets. The combination of coupled and decoupled (case C2) simulations allows obtaining an estimate of the local pressure losses for the cavity flow. Note that case C2 only includes the friction losses, and not the local losses. The Darcy-Weisbach equation that includes both friction losses and local losses is:

$$\Delta P = \left( \frac{fL}{D_h} + \sum C \right) \left( \frac{\rho W_{\text{avg}}^2}{2} \right) \quad (3)$$

where  $\sum C$  is the sum of the local loss coefficients. Note that, while the friction losses refer to the losses associated with fully-developed flow, the local losses are those due to developing flow conditions. As such,

the local losses include the entrance and exit losses. These losses are generally considered to be localised at the entrance and exit, although in reality they always occur over a certain distance in the flow direction. Substituting  $\Delta P = \Delta C_p(0.5\rho U_{10}^2)$  in Eq. (3) and solving for the sum of the local loss coefficients yields:

$$\sum C = \Delta C_p \left( \frac{U_{10}}{W_{\text{avg}}} \right)^2 - \frac{fL}{D_h} \quad (4)$$

Application of Eq. (4) for  $U_{10} = 10$  m/s yields values of  $\sum C$  from 4.5 (middle cavities) to 5.7 (edge cavities) for  $\theta = 0^\circ$ , and from 4.9 (middle) to 7.1 (edge) for  $\theta = 22.5^\circ$ , indicating a clear increase for the oblique wind direction. The ratio of local losses to total losses is quite constant: between 0.56 (middle) and 0.64 (edge) for  $\theta = 0^\circ$  and between 0.59 (middle) and 0.65 (edge) for  $\theta = 22.5^\circ$ .

## 7. Comparison with experimental results from previous studies

The CFD results for ACH and cavity air speed in this study seem quite large: ACH/ $U_{10}$  ranges between 120 and almost 250 s/mh for  $\theta = 0^\circ$ , and the corresponding dimensionless average cavity air speed  $W_{\text{avg}}/U_{10}$  ranges between 0.21 m/s for the edge cavities and 0.12 m/s for the middle cavities. These large values are attributed to the fact the opening areas are equal to the cavity cross-section. One could interpret this as the reference wind speed  $U_{10}$  being converted into a cavity air speed which is 5 to 10 times smaller. Although previous experimental studies were generally conducted for quite different building geometries, a comparison can be made between the CFD results and values from those experiments that most resemble the present situation.

Schwarz [5] measured air speed in a 40 mm cavity behind a 1.25 x 1.35 m<sup>2</sup> cladding panel with 8 mm thickness on a 18-storey building. As in the present study, the cavity had linear horizontal inlet and outlet openings spanning the entire width of the cavity. The measured cavity air speed  $W$  ranged from 0.2 to 0.6 m/s for a reference wind speed  $U_{\text{ref}}$  from 0 to 8 m/s, which corresponds to ACH values of about 500 to 1500 h<sup>-1</sup>. For  $U_{\text{ref}} = 8$  m/s, wind-induced cavity airflow is expected to dominate. In this situation, Schwartz's values are  $W/U_{\text{ref}} = 0.075$  and ACH/ $U_{\text{ref}} = 200$  s/mh. Note that  $U_{\text{ref}}$  is a reference wind speed which can not be directly related to  $U_{10}$  due to insufficient information about its measurement location.

Künzel and Mayer [7] reported measurements of air speed in different cavity geometries on a 3-storey building. The cavities were created by one or three consecutive 1.2 x 1.8 m<sup>2</sup> cladding panels with 10 mm thickness, yielding cavities of 1.8 or 5.4 m height. As in the present study, the cavities had horizontal openings spanning the entire cavity width. For a cavity depth of 20 mm and for  $U_{\text{ref}} > 3$  m/s and no solar radiation, they measured similar maximum values for both cavity heights:  $W$  up to 0.6 m/s, which corresponds to ACH values of 400 and 1200. The ratio  $W_{\text{avg}}/U_{\text{ref}}$  is 0.2 m/s and the corresponding values of ACH/ $U_{\text{ref}}$  are 133 and 400 s/mh.

The experimental values by Schwartz [5] and Künzel and Mayer [7] are actually very close to the CFD results in this study. Note that several other experimental studies have been published, but that in many cases the cavity opening geometry is (very) different, e.g. not horizontal openings spanning the entire cavity width but much smaller openings.

## 8. Discussion

The CFD approach used in this paper, with low-Re number modelling based on the Wolfstein model, cannot accurately reproduce friction coefficients (and therefore also cavity flow) in the transitional regime. For  $1000 < \text{Re} < 3500$ , errors in the predicted friction coefficients are larger than 25%. This imposed a strong limitation on the amount of reliable information that could be extracted from the CFD simulations: only results for which the cavity Re numbers were below 1000 or above 3500 were analysed.  $\text{Re} < 1000$  (in all cavities) occurred for  $U_{10} = 2$  m/s and  $\theta = 0^\circ$ , while  $\text{Re} > 3500$  (in all cavities) occurred for  $U_{10} = 10$  m/s and  $\theta = 0^\circ$  and  $22.5^\circ$ . It is important to note that in reality,  $U_{10}$  will often be in the 2-10 m/s range. This stresses the importance for improved low-Re number modelling that can accurately reproduce not only the laminar and turbulent but also the transitional flow regime in narrow facade cavities.

The CFD simulations in this paper were performed for smooth cavity walls, which is the only option in the presently used low-Re number modelling approach. While the friction coefficients are invariable with wall roughness for laminar cavity flow, they considerably increase with wall roughness for turbulent flow [14,15]. Rough walls will therefore cause lower cavity ventilation rates.

The present study only considered wind-induced airflow in the cavities. Future work should consider buoyancy-driven ventilation as well as the combination of wind-driven and buoyancy-driven ventilation. The

present study was limited to averaged wind speed and ACH. Future studies can include the effects of wind gusts and pulsating flow in the cavity. In addition, attention should be given to the problem of horizontal inhomogeneity of the atmospheric boundary layer in CFD simulations [32], in particular related to its effects on the wind pressure distribution on building facades.

The CFD simulations in this study were conducted following the best practice guidelines for CFD in the outdoor environment [18,19,20,32]. High-resolution computational grids were constructed based on grid-sensitivity analysis, with hexahedral cells adjacent to all wall boundaries and with adequate  $z^*$  values. Second-order discretisation schemes were used for all simulations. Validation with experimental data was performed for three different sub-configurations. The CFD results of cavity air speed and ACH were compared with those of previous experimental studies, indicating a favourable agreement. For future CFD validation studies, it would be beneficial to establish full-scale experimental data sets containing wind speed around the building, wind pressure coefficients at the facades and cavity air speed, accompanied by detailed measurements and reports of all influencing geometrical and meteorological parameters.

## 9. Summary and conclusions

This paper focused on coupled and decoupled RANS CFD simulations of wind-induced air flow in the narrow (23 mm) ventilated facade cavities of an isolated low-rise building. Accurately modelling the coupled wind flow and narrow cavity air flow is challenging because of the large differences in length scales and the resulting differences in flow behaviour: high-Re number turbulent flow around the building and low-Re number laminar, transitional and/or turbulent flow in the cavities. The CFD simulations were performed with the intention to identify the potential limitations of CFD for this type of application. This identification was supported by performing generic sub-configuration validation, which implies the decomposition of the actual problem or configuration into simpler, generic problems or configurations, which contain at least part of the features of the flow in the actual configuration. This validation study indicated that the wind velocities upstream of the building facade and the surface pressures on the windward facade can be predicted with good accuracy by steady RANS modelling with the realizable  $k-\epsilon$  model, while this is not the case for the wind velocities and surface pressures downstream of the windward facade, due to the specific deficiencies of steady RANS modelling. The validation study showed that low-Re number modelling with the two-layer zonal approach and the one-equation Wolfhstein model can reproduce cavity flow that is either clearly laminar ( $Re < 1000$ ) or turbulent ( $Re > 3500$ ), while it is deficient in the transitional regime: for  $1000 < Re < 3500$ , errors in the predicted friction coefficients are larger than 25%.

Results of the coupled simulations were analysed for those situations with cavity Re numbers outside the range 1000-3500. Distinct flow patterns and ACH variations were found along the windward facade. For a high reference wind speed  $U_{10}$  of 10 m/s and for wind perpendicular to the facade, the ratio  $ACH/U_{10}$  ranges between 120 and almost 250. These values compared favourably with those from past experimental studies. Comparing the results from the coupled and decoupled simulations allowed to assess the local losses (entrance and exit losses) of the cavities. The sum of the entrance and exit loss coefficients for  $\theta = 0^\circ$  ranges between 4.5 (middle cavities) and 5.7 (edge cavities), and for  $\theta = 22.5^\circ$  between 4.9 and 7.1.

While this study has shown that the RANS low-Re number modelling approach used is capable of reproducing both the laminar and turbulent flow in narrow ventilated facade cavities. Future work should focus on adapting this approach to accurately model cavity flow in the transitional regime.

## Acknowledgements

The authors want to express their gratitude to Dr. Hartwig Künzel, head of the Hygrothermal Unit of the Fraunhofer-Institut für Bauphysik in Holzkirchen, Germany, for providing valuable literature information that was hard to find. Gratitude is also expressed to the Finn Krogstads Fund for travelling funds that allowed the international collaboration.

## References

- [1] T.K. Stovall, A.N. Karagiozis, Airflow in the ventilation space behind a rain screen wall, in: Proceedings of Thermal Performance of the Exterior Envelopes of Buildings IX, ASHRAE Buildings IX, Clearwater Beach, FL, USA, 2004.
- [2] D. Davidovic, J. Srebric, E.F.P. Burnett, Modeling convective drying of ventilated wall chambers in building enclosures, *International Journal of Thermal Sciences* 45 (2006) 180-189.

- [3] S. Gnoth, P. Häupl, H. Fechner, New aero-thermo-hygric behaviour of building structures with open and closed cavities, in: Proceedings of Building Physics Conference, Laboratory of Building Physics, Katholieke Universiteit Leuven, Leuven, Belgium, 2008, pp. 29-32.
- [4] H.M. Künzl, A.N. Karagiozis, M. Kehrler, Assessing the benefits of cavity ventilation by hygrothermal simulation, in: Proceedings of Building Physics Conference, Laboratory of Building Physics, Katholieke Universiteit Leuven, Leuven, Belgium, 2008, pp. 17-21.
- [5] B. Schwarz, Witterungsbeanspruchung von Hochhausfassaden (in German), HLH (Heizung, Lüftung/Klimatechnik, Haustechnik) 24(12) (1973) 376–384.
- [6] W. Popp, E. Mayer, H. Künzl, Untersuchungen über die Belüftung des Luftraumes hinter vorgesetzten Fassadenbekleidung aus kleinformigen Elementen, Fraunhofer Institut für Bauphysik, Forschungsbericht BHo 22/80, April, 1980.
- [7] H. Künzl, E. Mayer, Untersuchung über die notwendige Hinterlüftung an Außenwandbekleidung aus großformatigen Bauteilen, Schriftenreihe Bundesminister für Raumordnung, Bauwesen, und Städtebau, 3/1983.
- [8] K. Sandin, Cavity wall moisture and temperature conditions (In Swedish), R43, Statens råd för byggnadsforskning, Stockholm, Sweden, 1981.
- [9] C. Gudum, Moisture transport and convection in building envelopes – ventilation in light weight outer walls, PhD thesis, Technical University of Denmark, Copenhagen, Denmark, 2003.
- [10] J. Straube, R. VanStraaten, E. Burnett, C. Schumacher, Review of literature and theory, Report #1, ASHRAE 1091 – Development of Design Strategies for Rainscreen and Sheathing Membrane Performance in Wood Frame Walls, Building Engineering Group, University of Waterloo, 2004.
- [11] J.P. Piñon, D. Davidovic, E. Burnett, J. Srebric, Ventilated cavities in screen-type enclosure wall systems (RP 1091), In: Proceedings of Thermal Performance of the Exterior Envelopes of Buildings IX, ASHRAE Buildings IX, Clearwater, FL, USA, 2004.
- [12] C. Schumacher, S. Xing, E. Burnett, Ventilation drying in screen-type wall systems: a physical demonstration, Report #3, ASHRAE 1091 – Development of Design Strategies for Rainscreen and Sheathing Membrane Performance in Wood Frame Walls, Building Engineering Group, University of Waterloo, 2004.
- [13] E.F.P. Burnett, J.F. Straube, Vents, ventilation, drying and pressure moderation, Research Report. Canada Mortgage and Housing Corporation, 1995.
- [14] I.E. Idelchik, Handbook of Hydraulic Resistance, third ed., CRC Press Inc., 1994.
- [15] ASHRAE. Handbook of Fundamentals, American Society of Heating, Refrigerating and Airconditioning Engineers, 2009.
- [16] D. Costola, B. Blocken, J.L.M. Hensen, Overview of pressure coefficient data in building energy simulation and airflow network programs, Building and Environment 44(10) (2009) 2027-2036.
- [17] J. Wieringa, Updating the Davenport roughness classification, Journal of Wind Engineering and Industrial Aerodynamics 41-44 (1992) 357-368.
- [18] J. Franke, A. Hellsten, H. Schlünzen, B. Carissimo, Best practice guideline for the CFD simulation of flows in the urban environment, COST Action 732: Quality Assurance and Improvement of Microscale Meteorological Models, 2007.
- [19] Y. Tominaga, A. Mochida, R. Yoshie, H. Kataoka, T. Nozu, M. Yoshikawa, T. Shirasawa, AIJ guidelines for practical applications of CFD to pedestrian wind environment around buildings, Journal of Wind Engineering and Industrial Aerodynamics 96(10,11) (2008) 1749–1761.
- [20] M. Casey, T. Wintergerste, ERCOFTAC Best Practice Guidelines, Special Interest Group on Quality and Trust in Industrial CFD, 2000.
- [21] Fluent Inc. Fluent 6.3 User's Guide. Lebanon, US, 2006.
- [22] T. Defraeye, B. Blocken, J. Carmeliet, CFD analysis of convective heat transfer at the surfaces of a cube immersed in a turbulent boundary layer, International Journal of Heat and Mass Transfer, (2010) 53(1-3): 297-308.
- [23] M. Wolfhstein, The velocity and temperature distribution of one-dimensional flow with turbulence augmentation and pressure gradient, International Journal of Heat and Mass Transfer 12 (1969) 301-318.
- [24] T.H. Shih, W.W. Liou, A. Shabbir, J. Zhu, A new k-ε eddy-viscosity model for high Reynolds number turbulent flows – model development and validation, Computers and Fluids 24(3) (1995) 227-238.
- [25] B. Blocken, T. Defraeye, D. Derome, J. Carmeliet, High-resolution CFD simulations of forced convective heat transfer coefficients at the facade of a low-rise building, Building and Environment 44(12) (2009) 2396-2412.
- [26] B. Blocken, J. Carmeliet, Pedestrian wind conditions at outdoor platforms in a high-rise apartment building: generic sub-configuration validation, wind comfort assessment and uncertainty issues, Wind and Structures 11(1) (2008) 51-70.

- [27] P.J. Richards, R.P. Hoxey, B.D. Connell, D.P. Lander, Wind-tunnel modelling of the Silsoe Cube, *Journal of Wind Engineering and Industrial Aerodynamics* 95(9-11) (2007) 1384-1399.
- [28] W.H. Snyder, Guideline for fluid modeling of atmospheric diffusion, US Environmental Protection Agency Report EPA-600/8-81-009, 1981.
- [29] B. Blocken, T. Stathopoulos, J. Carmeliet, Wind environmental conditions in passages between two long narrow perpendicular buildings, *Journal of Aerospace Engineering – ASCE* 21(4) (2008) 280-287.
- [30] B.E. Launder, D.B. Spalding, The numerical computation of turbulent flows, *Computer Methods in Applied Mechanics and Engineering* 3 (1974) 269-289.
- [31] T. Cebece, P. Bradshaw, *Momentum Transfer in Boundary Layers*, Hemisphere Publishing Corporation, New York, 1977.
- [32] B. Blocken, T. Stathopoulos, J. Carmeliet, CFD simulation of the atmospheric boundary layer: wall function problems, *Atmospheric Environment* 41(2) (2007) 238-252.
- [33] S. Murakami, Comparison of various turbulence models applied to a bluff body, *Journal of Wind Engineering and Industrial Aerodynamics* 46&47 (1993) 21-36.
- [34] Y. Tominaga, A. Mochida, S. Murakami, S. Sawaki, Comparison of various revised  $k-\epsilon$  models and LES applied to flow around a high-rise building model with 1:1:2 shape placed within the surface boundary layer, *Journal of Wind Engineering and Industrial Aerodynamics* 96(4) (2008) 389-411.
- [35] F.M. White, *Viscous Fluid Flow*, third ed., McGraw-Hill, 1974.
- [36] F.P. Incropera, D.P. DeWitt, *Fundamentals of Heat and Mass Transfer*, fifth ed., Chichester, Wiley, 2001.
- [37] H. Schlichting, *Boundary-layer Theory*, seventh ed., McGraw-Hill, London, 1979.
- [38] T. van Hooff, B. Blocken, Coupled urban wind flow and indoor natural ventilation modelling on a high-resolution grid: A case study for the Amsterdam ArenA stadium, *Environmental Modelling & Software* 25(1) (2010) 51-65.
- [39] P.J. Richards, R.P. Hoxey, Appropriate boundary conditions for computational wind engineering models using the  $k-\epsilon$  turbulence model, *Journal of Wind Engineering and Industrial Aerodynamics* 46&47 (1993) 145-153.
- [40] B. Blocken, J. Carmeliet, T. Stathopoulos, CFD evaluation of the wind speed conditions in passages between buildings – effect of wall-function roughness modifications on the atmospheric boundary layer flow, *Journal of Wind Engineering and Industrial Aerodynamics* 95(9-11) (2007) 941-962.
- [41] T. Stathopoulos, R. Storms, Wind environmental conditions in passages between buildings, *Journal of Wind Engineering and Industrial Aerodynamics* 24 (1986) 19–31.
- [42] B. Blocken, J. Carmeliet, On the validity of the cosine projection in wind-driven rain calculations on buildings, *Building and Environment* 41(9) (2006) 1182–1189.
- [43] M. Abuku, B. Blocken, K. Nore, J.V. Thue, J. Carmeliet, S. Roels, On the validity of numerical wind-driven rain simulation on a rectangular low-rise building under various oblique winds, *Building and Environment* 44(3) (2009) 621-632.
- [44] B. Blocken, P. Moonen, T. Stathopoulos, J. Carmeliet, A numerical study on the existence of the Venturi-effect in passages between perpendicular buildings, *Journal of Engineering Mechanics – ASCE* 134(12) (2008) 1021-1028.
- [45] B. Blocken, J. Carmeliet, The influence of the wind-blocking effect by a building on its wind-driven rain exposure, *Journal of Wind Engineering and Industrial Aerodynamics* 94(2) (2006) 101-127.

**Figures**

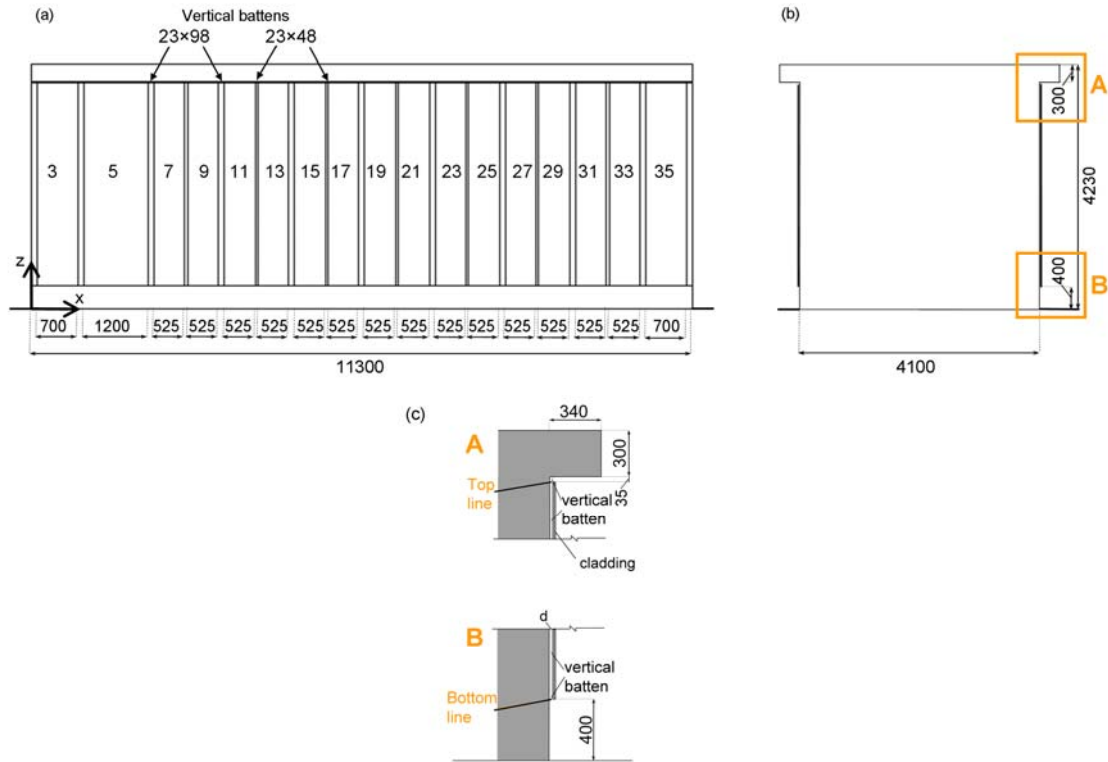


Fig. 1. (a) West facade of the low-rise building model. The numbers and the width of the individual cavities are indicated, as well as the cross-sectional dimensions of the vertical battens. (b) North facade with indication of two details A and B. (c) Details A and B of cross-section at top and bottom of cavity. The position of two horizontal lines (top line and bottom line, along the length of the facade) along which results will be presented, are indicated. Dimensions in mm.

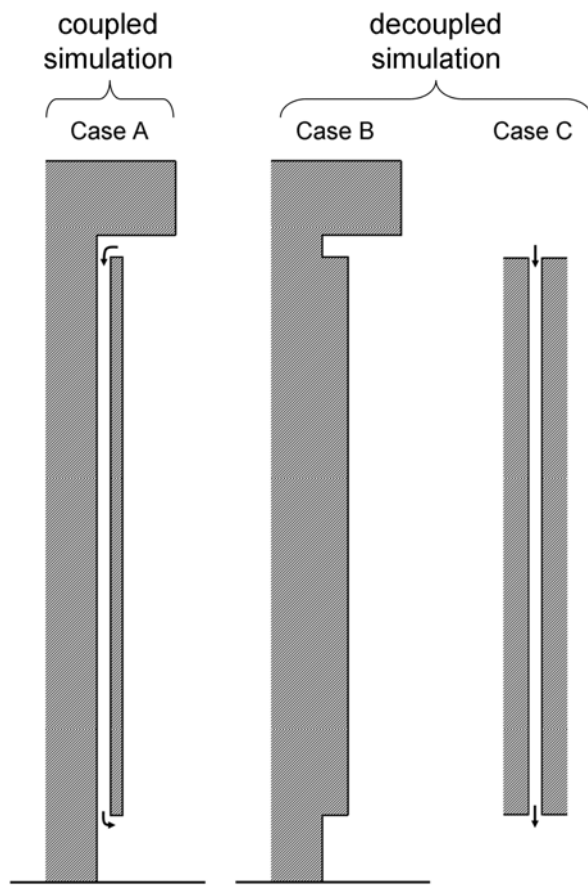


Fig. 2. Schematic representation of cavity configurations for coupled (A) and decoupled (B+C) simulations.

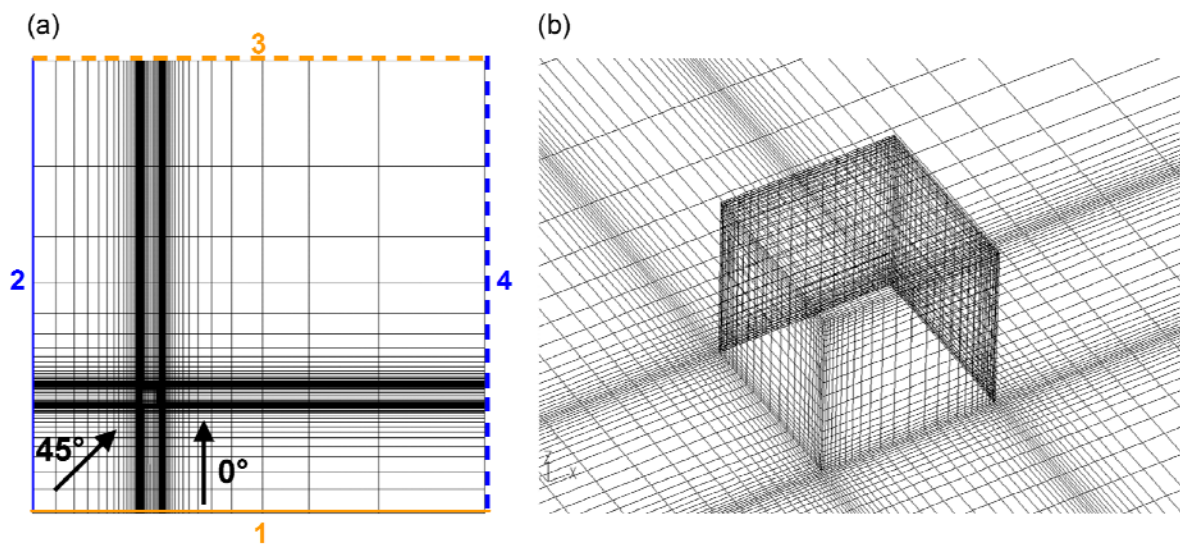


Fig. 3. (a) Grid at the bottom of the computational domain, and indication of the vertical boundary planes (1-4) of the domain. (b) Grid at the surfaces of the building and part of the ground surface.

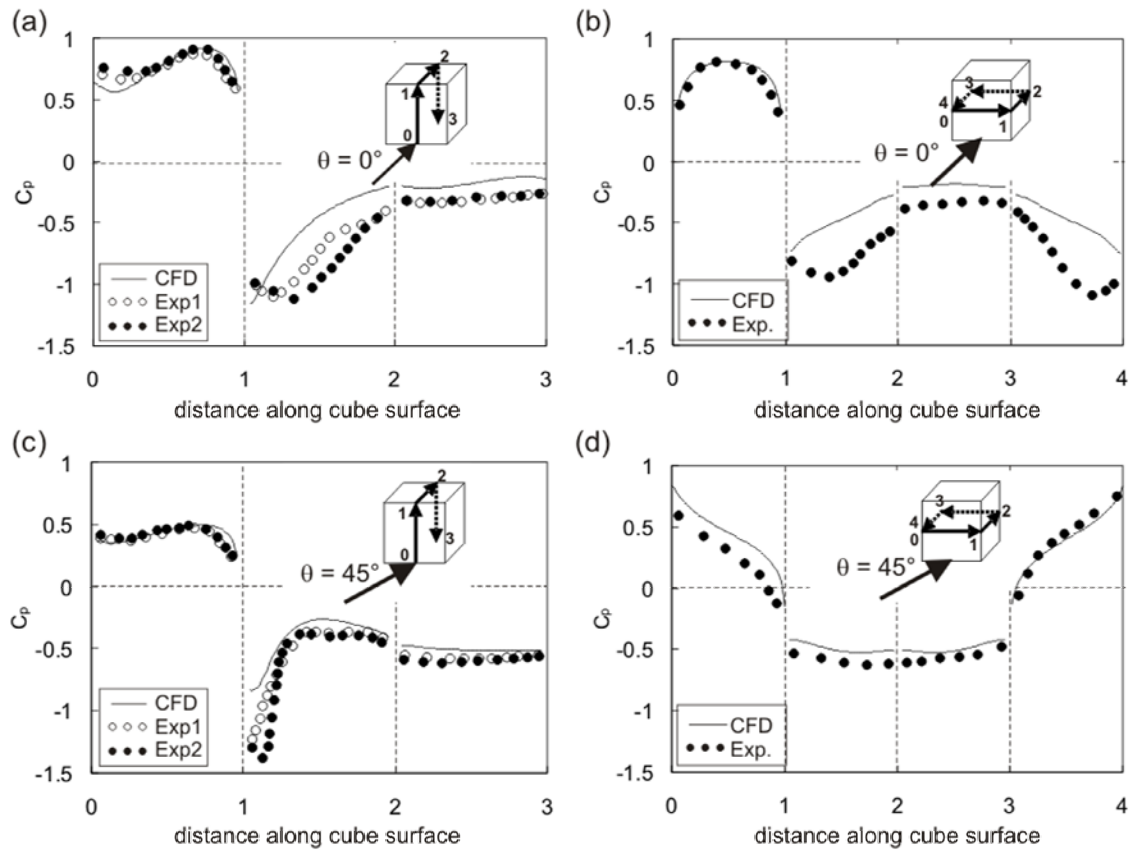


Fig. 4. Comparison between experiments and CFD results for cubic building: mean pressure coefficient  $C_p$  along (a) vertical trajectory 0-1-2-3 for  $\theta = 0^\circ$ ; (b) horizontal trajectory 0-1-2-3-4 for  $\theta = 0^\circ$ ; (c) same as (a) but for  $\theta = 45^\circ$ ; (d) same as (b) but for  $\theta = 45^\circ$ .

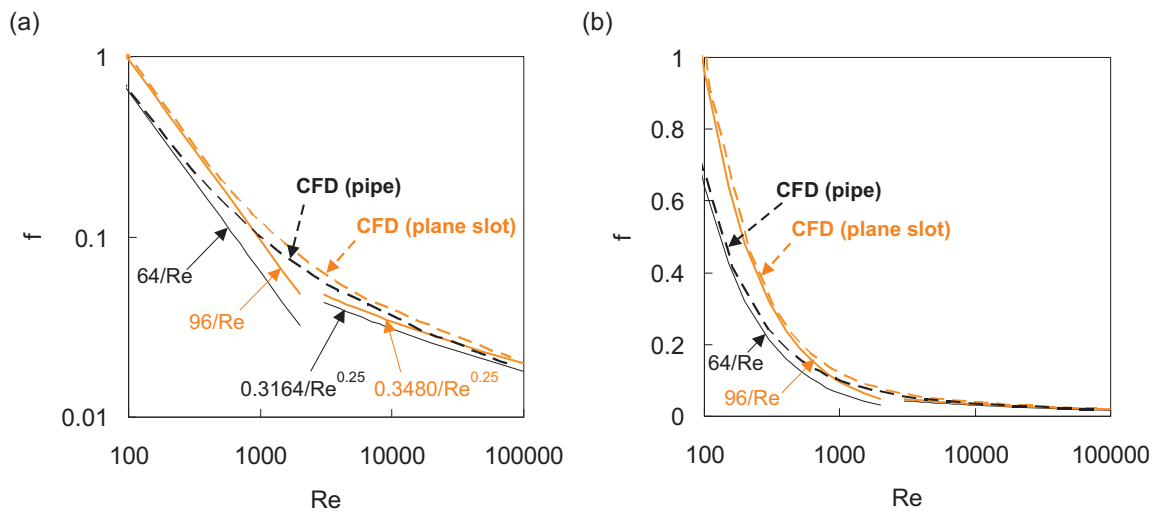


Fig. 5. Friction factors for fully-developed pipe and plane slot flow: comparison between CFD and theoretical/empirical expressions. (a) Double-logarithmic graph; (b) semi-logarithmic graph.

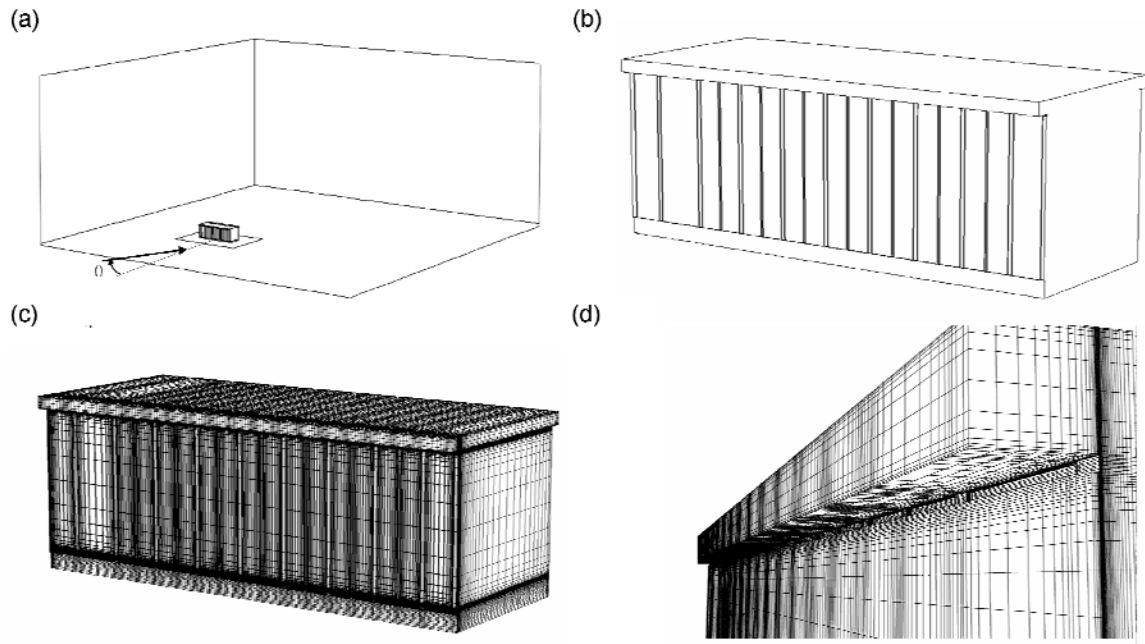


Fig. 6. (a) Building model in computational domain. (b) Building model with details of roof overhang and individual cavities separated by battens. (c) Computational grid on the building surfaces. (d) Detail of computational grid near the upper part of the cavities. The vertical battens, separating the cavities, are visible just below the roof overhang.

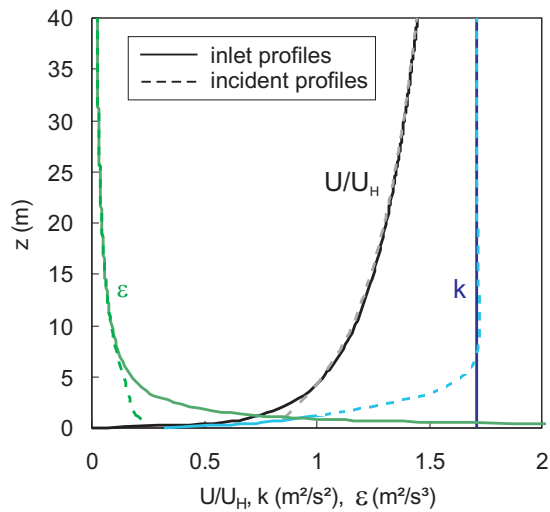


Fig. 7. Comparison between inlet and incident vertical profiles of dimensionless mean wind speed  $U/U_H$ , turbulent kinetic energy  $k$  and turbulence dissipation rate  $\epsilon$ .

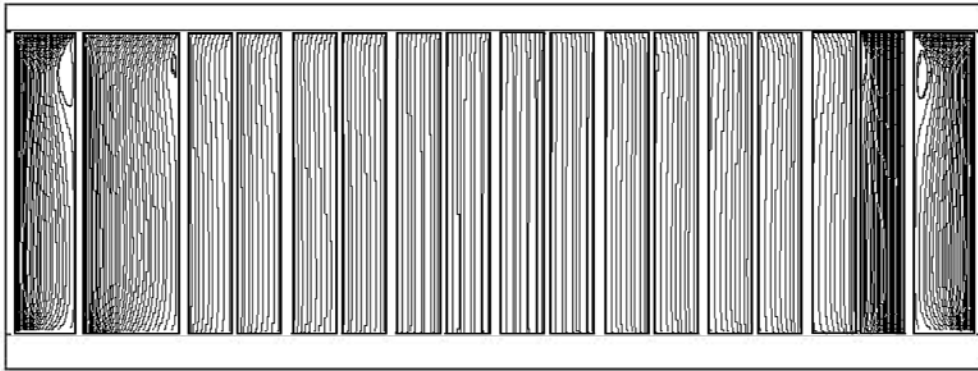


Fig. 8. Streamlines in the mid-planes of the cavities for  $\theta = 0^\circ$ . Overall cavity flow is from top to bottom.

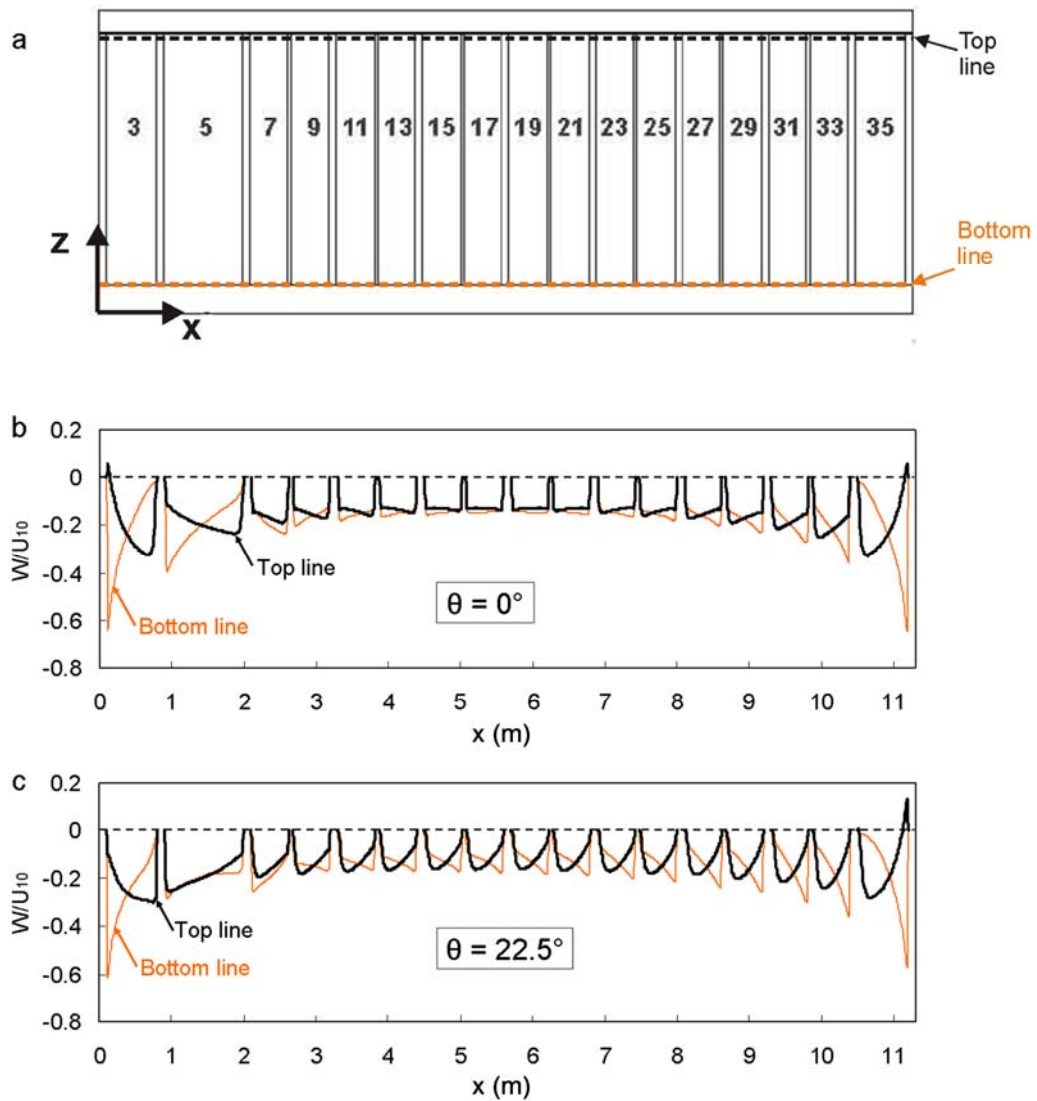


Fig. 9. (a) Building facade with cavities. (b-d) Ratio of vertical velocity component  $W$  to reference wind speed  $U_{10}$  for each cavity (top and bottom), for  $U_{10} = 10$  m/s and for  $\theta = 0^\circ$  and  $22.5^\circ$ .

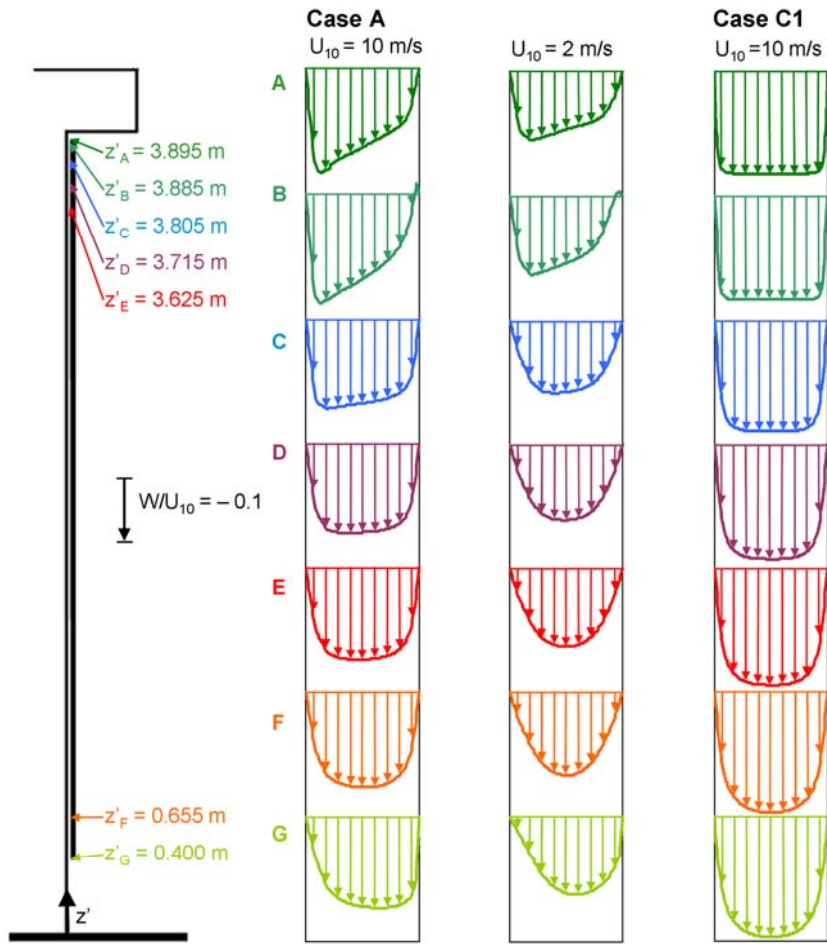


Fig. 10. Profiles of the ratio  $W/U_{10}$  across the cavity depth for coupled (case A, for  $U_{10} = 10$  and  $2 \text{ m/s}$ ) and decoupled (case C1, for  $U_{10} = 10 \text{ m/s}$ ) simulation, for the middle cavity (nr. 19, see Fig. 1a) and for  $\theta = 0^\circ$ .

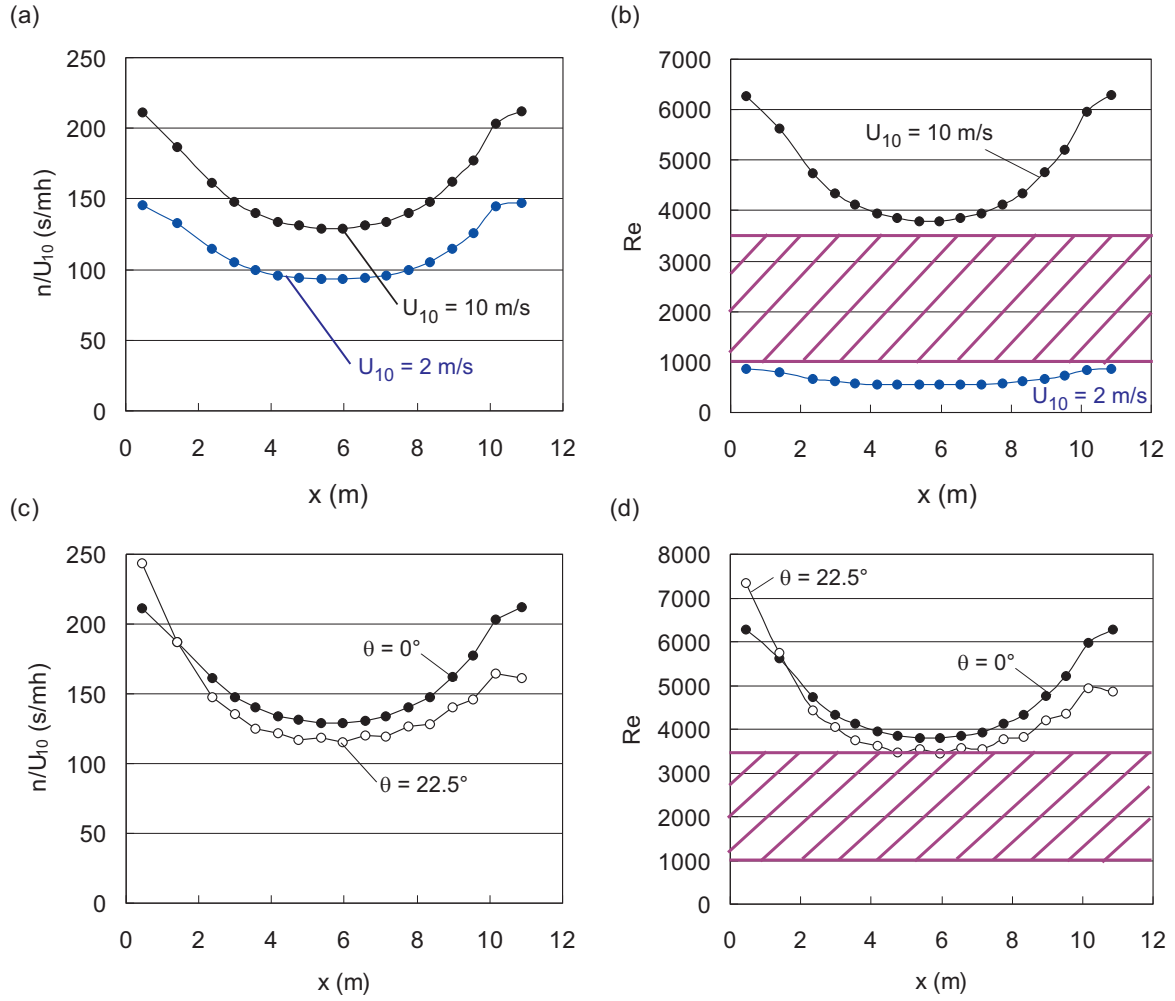


Fig. 11. (a) Ratio of cavity air change rate  $n$  and reference wind speed  $U_{10}$ , for  $\theta = 0^\circ$  and  $U_{10} = 2$  and  $10$  m/s. (b) Cavity Reynolds numbers for same  $\theta$  and  $U_{10}$ . The hatched area indicates the transitional Re number region in which low-Re number modelling fails. (c) Same as (a), but for  $U_{10} = 10$  m/s and  $\theta = 0^\circ$  and  $22.5^\circ$ . (d) Same as (b), but for  $U_{10} = 10$  m/s and  $\theta = 0^\circ$  and  $22.5^\circ$ .

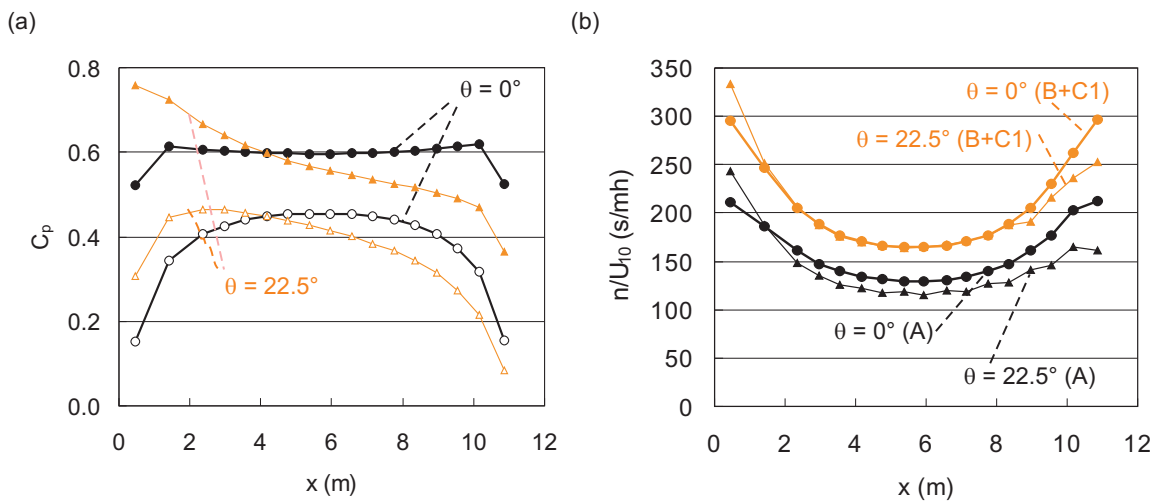


Fig. 12. (a) Pressure coefficient  $C_p$  from decoupled simulations, at the position of the top and bottom openings, for  $U_{10} = 10$  m/s and  $\theta = 0^\circ$  and  $22.5^\circ$ . (b) Comparison of  $n/U_{10}$  obtained from the coupled (A) versus decoupled (B+C1) simulations, for  $U_{10} = 10$  m/s and  $\theta = 0$  and  $22.5^\circ$ .